

In Silico High-Throughput Design and Prediction of Structural and Electronic Properties of Low-Dimensional Metal–Organic Frameworks

Zeyu Zhang, Dylan S. Valente, Yuliang Shi, Dil K. Limbu, Mohammad R. Momeni,* and Farnaz A. Shakib*



Cite This: *ACS Appl. Mater. Interfaces* 2023, 15, 9494–9507



Read Online

ACCESS |

Metrics & More

Article Recommendations

Supporting Information

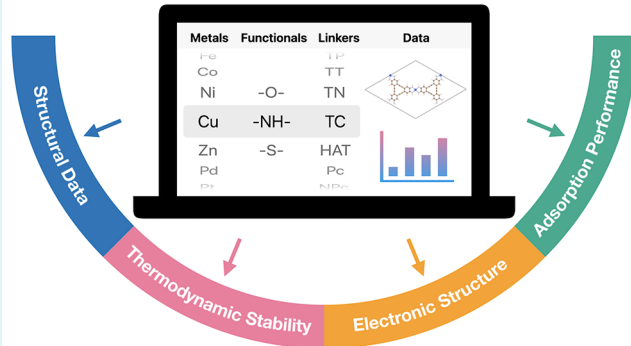
ABSTRACT: The advent of π -stacked layered metal–organic frameworks (MOFs), which offer electrical conductivity on top of permanent porosity and high surface area, opened up new horizons for designing compact MOF-based devices such as battery electrodes, supercapacitors, and spintronics. Permutation of structural building blocks, including metal nodes and organic linkers, in these electrically conductive (EC) materials, results in new systems with unprecedented and unexplored physical and chemical properties. With the ultimate goal of providing a platform for accelerated material design and discovery, here we lay the foundations for the creation of the first comprehensive database of EC-MOFs with an experimentally guided approach. The first phase of this database, coined EC-MOF/Phase-I, is composed of 1,057 bulk and monolayer structures built by all possible combinations of experimentally reported organic linkers, functional groups, and metal nodes. A high-throughput screening (HTS) workflow is constructed to implement density functional theory calculations with periodic boundary conditions to optimize the structures and calculate some of their most relevant properties. Because research and development in the area of EC-MOFs has long been suffering from the lack of appropriate initial crystal structures, all of the geometries and property data have been made available for the use of the community through an online platform that was developed during the course of this work. This database provides comprehensive physical and chemical data of EC-MOFs as well as the convenience of selecting appropriate materials for specific applications, thus accelerating the design and discovery of EC-MOF-based compact devices.

KEYWORDS: low-dimensional materials, metal–organic frameworks (MOFs), electrical conductivity, computationally ready databases, high-throughput screening

1. INTRODUCTION

In the last two decades, metal–organic frameworks (MOFs) have constituted one of the fastest-growing fields in chemistry and materials science¹ with a wide range of applications in adsorption,² separation,³ and catalysis,^{4–6} to name a few.⁷ MOFs are a class of porous crystalline materials obtained through a process usually referred to as reticular synthesis.⁸ Selected metal nodes and organic linkers, also called secondary building units (SBUs), are connected via strong coordination bonds to form ordered and permanently porous architectures.⁹ The modular nature of MOFs provides many opportunities to tailor their physical and chemical characteristics, which has led to more than 110,000 MOFs reported to date according to the Cambridge Structural Database (CSD).¹⁰ Traditional MOFs are mostly classified as insulators with wide band gaps, which limits their further utilization in electrical and optical devices.¹¹

EC-MOF Database / Phase I



The discovery of electrically conductive (EC) π -stacked layered MOFs, also referred to as two-dimensional (2D) MOFs, in 2012 opened a new research direction in this area.¹² Ever since, new 2D MOFs with excellent electrical conductivity and magnetic properties have been reported and introduced as viable candidates for field-effect transistors,¹³ supercapacitors,¹⁴ superconductors,¹⁵ spintronics,¹⁶ and cathode materials in different metal-ion batteries.¹⁷ Normally, EC-MOFs contain ortho-substituted π -conjugated organic linkers coordinated to

Received: December 16, 2022

Accepted: January 26, 2023

Published: February 7, 2023



(usually) early 3d transition metal nodes, forming extended π -conjugated 2D sheets. Weak van der Waals interactions allow the stacking of these 2D sheets to form bulk crystalline materials with one-dimensional channels in the stacking direction. This architecture provides necessary paths for charge transport along both in-plane and out-of-plane directions.¹⁸ Various building blocks for EC-MOFs are reported in the literature, and as mentioned earlier, MOFs in general can be rationally designed by choosing different combinations of organic linkers and metal node building blocks. However, considering the vast and virtually infinite chemical space of MOFs, it is extremely labor-intensive and time-consuming to synthesize all different combinations of building blocks to find the best materials for any desired application. A more efficient and systematic way is to create a comprehensive database of different classes of MOFs and then screen them for desired applications using accelerated high-throughput screening (HTS) techniques.¹⁹ Chung et al.²⁰ created a computation-ready, experimental (CoRE) MOF database with over 5,000 MOFs based on CSD in 2014. Various other data sets have evolved from the CoRE MOF database, such as CoRE MOF 2014+DDEC,²¹ where partial atomic charges were determined for 50% of the reported MOFs using density functional theory (DFT) calculations as well as CoRE MOF 2014-DFT-optimized,²² where DFT geometric relaxation was performed for 879 structures. The CoRE MOF database itself was updated in 2019 with the total number of MOFs being increased to 14,000.²³ On the other hand, the Cambridge Crystallographic Data Centre (CCDC) created a MOF subset based on existing CSD that contains the largest number of experimentally synthesized MOFs to date.²⁴ A total number of 69,666 MOFs were gathered in this subset after screening the original CSD based on seven different criteria and removing solvent molecules from the MOF pores. A more recent work by Rosen et al.²⁵ in 2021 introduced a new database called the Quantum MOF (QMOF) database containing 15,713 MOFs that were successfully optimized and analyzed by HTS periodic DFT workflows. Not only were experimental MOFs collected in different databases, but a hypothetical MOF database was also recently built by Wilmer et al.²⁶ where 137,953 new MOFs were created from a combination of 102 different building blocks. More than 300 candidates were selected with excellent methane storage capacity. More recently, Gharagheizi et al.²⁷ created a collection of \sim 20,000 1D MOFs curated from the CSD non-disordered MOF subset that includes \sim 2,000 electrically conductive structures. All these carefully curated databases allow the selection of materials with desired properties and performance for specific applications by the fast screening of hundreds and/or thousands of structures. However, they all exclude or at best partially include π -stacked layered EC-MOFs because they are a very new class of materials. Considering the wide potential of EC-MOFs, it is crucial to first build a comprehensive database for them, which will then allow various HTS techniques to be routinely applied in order to accelerate materials design and discovery. Here, we report the first installation of our experimentally guided, computationally ready database of EC-MOFs, coined EC-MOF/Phase-I, containing 1,057 bulk and monolayer structures. This database is available for community use via the online platform developed during the course of this study at <https://ec-mof.njit.edu>. All of the structures in this database follow a comprehensive naming rule as shown generally and with an example in Figure 1. This naming rule, which will be

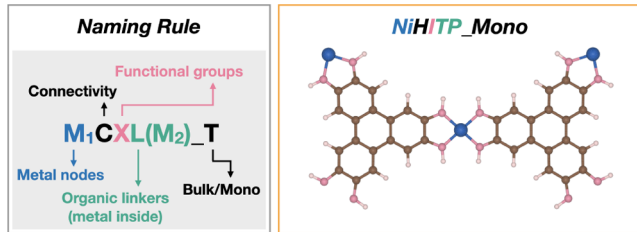


Figure 1. Naming rules used for the structures included in EC-MOF/Phase-I database (left) and an example of a built NiHITP crystal structure (right).

explained in the next section, gives enough information to the user about the nature of metal nodes, functional groups, organic linkers, connectivity between building blocks, and types of unit cells. In this way, the users can easily have access to the desired structure in the database through the choice of each of these components where they can build and download their structure. Furthermore, the users not only have access to the crystal structures but also geometric data and electronic properties obtained using our in-house HTS workflow. We will provide the details of the applied procedures and developed software for building the database in the next section. In section 3, we will present the results of our HTS investigation of the carefully curated 1,057 bulk and monolayer systems. Section 4 outlines future directions with concluding remarks given in section 5.

2. COMPUTATIONAL DEVELOPMENTS

2.1. EC-MOFs from Literature. In this work, we first performed a thorough literature survey and summarized all reports on EC-MOFs that have been either synthesized and/or theoretically investigated. With the intention of developing a structure creation tool for the automatic generation of initial crystal structures of EC-MOFs for our database, we initially focused on identifying structural features that induce the highest electrical conductivity. Accordingly, we restricted the first version of our database to π -stacked EC-MOFs with planar layers and extended π -conjugation through organic linkers and metal nodes with 2+ oxidation state, allowing for effective d- π conjugation. Notably, Hofmann-type MOFs are excluded from the first version of our database because, depending on the nature of the coordinative bonds, they can form 3D structures where π -stacking can occur along the in-plane rather than out-of-plane direction. Moreover, the presence of Pt²⁺ nodes can disturb the in-plane electrical conductivity in some of these MOFs.^{28,29} Other classes of MOFs were excluded on the basis of the presence of twists in the layers,³⁰ which can disrupt extended in-plane conjugation; the presence of bi- and trinuclear metal nodes,³¹ which can disrupt effective in-plane d- π conjugation; and >4 Å interlayer distances,³² which reduce out-of-plane π - π interactions drastically. The subset of EC-MOFs gathered in our database follow the color-coded naming rule depicted in Figure 1 based on three structural building components including organic linkers, metal nodes, and functional groups. Figure 2 demonstrates all of the structural components used in building the EC-MOF/Phase-I database. The eight metal nodes including Mn, Fe, Co, Ni, Cu, Zn, Pd, and Pt are identified by M_1 in our naming rule, while X denotes three functional groups, as H for hydroxyl, I for imino, and T for thiol, that connect to the metal nodes. The linker subset of structural

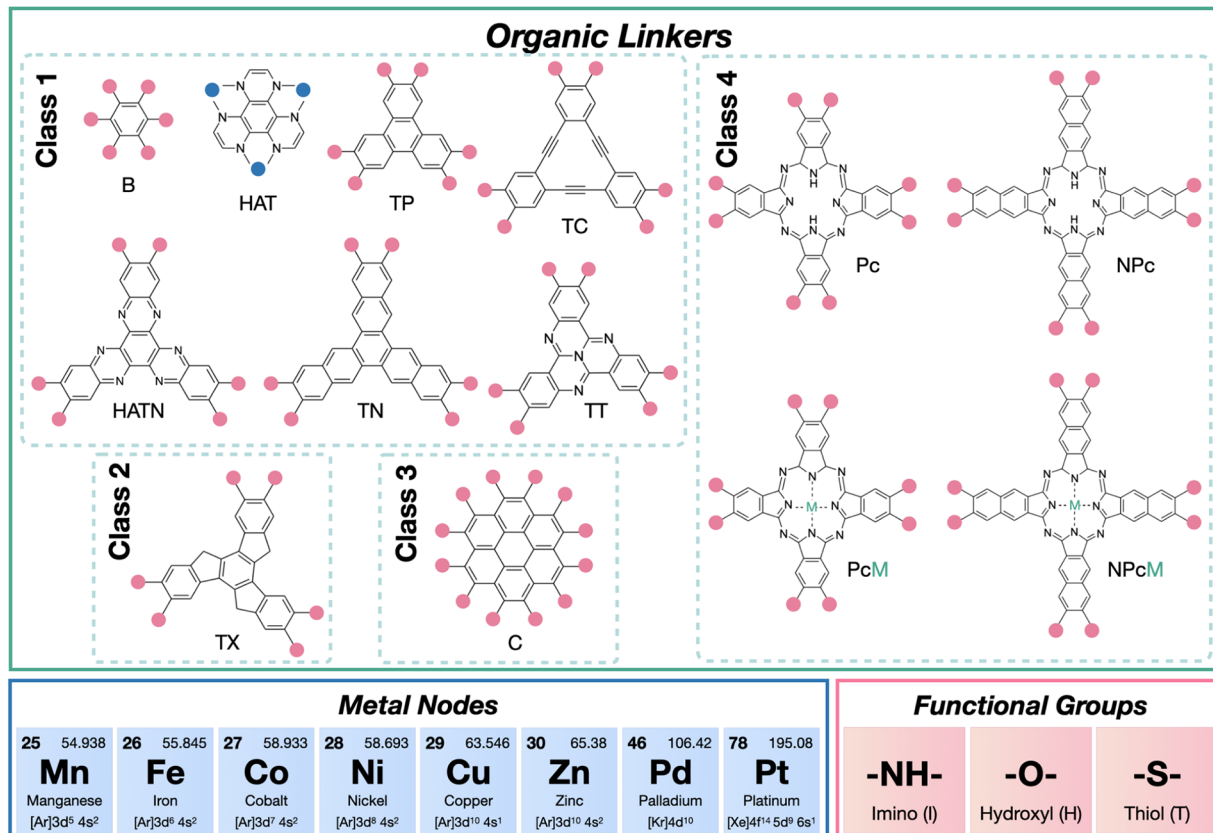


Figure 2. Three subsets of structural building components including organic linkers (classes 1–4), metal nodes, and functional groups (green, blue, and pink boxes, respectively). Connecting sites of organic linkers to the metal and functional groups are highlighted by blue and pink dots, respectively.

building components, denoted as L in our naming rule, consists of 11 organic linkers including benzene (B), triphenylene (TP), trinaphthylene (TN), truxene (TX), coronene (C), tribenzocyclyne (TC), tetraazanaphthotetraphene (TT), hexaaazatriphenylene (HAT), hexaaazatinaphthalene (HATN), phthalocyanine (Pc), and naphthalocyanine (NPc). Pc and NPc linkers can accommodate one more transition metal atom inside. Transition metals including Fe, Co, Ni, Cu, Zn, and Pd are observed in the synthesized Pc- and NPc-based MOFs;^{33–38} therefore, PcM and NPcM with six different interior metal centers are considered. The connections between metal nodes and organic linkers happen through 3, 4, or 6 bidentate sites. Accordingly, 6, 8, or 12 functional groups are placed around one linker. This is identified with C (as in connectivity) in our naming rule, which can be replaced with H for hexa, O for octa, and P for per. Furthermore, M_2 is the metal atom inside the organic linkers, if it exists. At last, T indicates the type of unit cell, which has two options, bulk or monolayer. Naturally, some of the resulting structures originated from reported works, but most are hypothetical. Hence, our building strategy screens all combinations of the building blocks but keeps a tight connection between experimental and hypothetical structures.

2.2. Crystal Structure Producer. On the basis of the criteria established in the previous section, we identified four different classes of EC-MOFs according to the shape and connectivity of the organic linkers as demonstrated in Figure 3. An in-house structure building tool, coined Crystal Structure Producer (CrySP), is developed to create periodic structures of

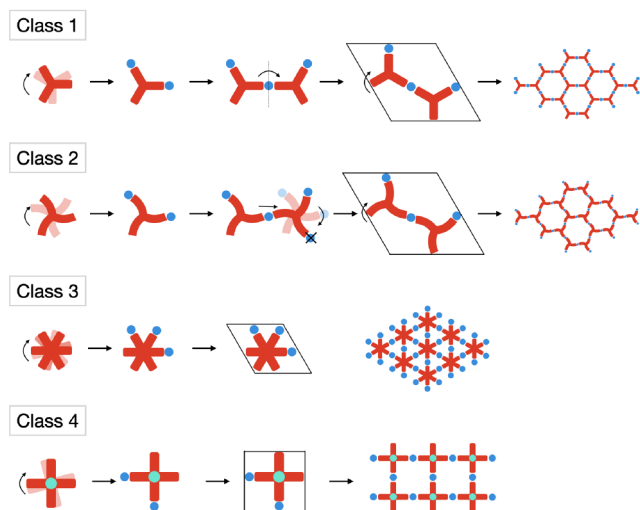


Figure 3. Building logic of CrySP for four different classes of MOFs created in this work. Classification of organic linkers is given in Figure 2 with our formulations for the calculation of cell vectors of different classes provided in the Supporting Information. In this figure blue represents metal nodes, red represents organic linkers, and green represents metal atoms located inside the linkers.

EC-MOFs that fit into these four geometric classes without any minimization using generic force fields. The optimization of all structures was carried out at the DFT level, which will be explained in the next section. The CrySP algorithm starts by

rotating the organic linker to the desired position, and then functional groups are placed around the organic linker according to the connectivity of the linker. Next, metal nodes are added according to the bond length between metals and functional groups, which is specified in advance. After necessary transformations, the structure is rotated to fit into the specified unit cell. Structures in our database, coined EC-MOF/Phase-I, can be classified into 3 different lattices, including honeycomb (hcb), hexagonal (hxl), and square (sql) lattices.³⁹ We further divide hxl structures into 2 classes due to the unique building procedure needed for TX-based MOFs. The details of the building procedures of the four classes may vary as schematically shown in Figure 3. In class 1, CrySP calls up the XYZ coordinates of the desired organic linker and places metal nodes around it in appropriate positions and distances. Then, the entire structure is reflected along the *y* axis. The last steps are moving and rotating the structure to fit into the specified unit cell. In class 2, the reflection step is replaced by moving and rotating operations due to the special symmetry of the linker which then requires removing the extra metal atom. In classes 3 and 4, once the organic linker is placed at the center of the unit cell, functional groups and metals are added around the organic linker without any transformational operations. At the same time, CrySP calculates cell parameters for each class of materials by taking the positions of the metal nodes as reference points. The mathematical details can be found in the Supporting Information, section S1 and Figure S1. Finally, CrySP creates the structures in the desired formats including XYZ, Crystallographic Information file (CIF), or POSCAR. The resulting structures at this stage are all monolayers. To optimize the monolayer structures, a vacuum space of 20 Å is added to the *c* direction of the unit cells. Bulk structures, containing 2 layers in the unit cell, are created with a fixed interlayer distance of 3.25 Å along the out-of-plane direction while considering different crystal packings known as AA or AB stackings.⁴⁰ Accordingly, a total of 1,072 structures are created by CrySP and gathered in the first version of our EC-MOF database.

2.3. Details of High-Throughput Screening Workflows and Periodic Electronic Structure Calculations. To maximize the advantages of EC-MOF/Phase-I, we apply high-throughput screening (HTS) techniques to explore different properties of these materials (see Figure 4). Multiple steps of periodic density functional theory (DFT) calculations are performed in our HTS workflows, which are all carried out using the Vienna ab initio simulation package (VASP) version 5.4.4.^{41–44} Interactions between electrons and ions are described by projector-augmented wave (PAW) potentials^{45,46} with a cutoff energy of 500 eV. Spin-polarized calculations are performed for all systems, resulting in high-spin states, rather than low-spin states, being the most common for all structures. The Perdew–Burke–Ernzenhof (PBE) functional with Grimmes damped D3 dispersion correction within the generalized gradient approximation (GGA) formalism^{47,48} was employed in this work, which provides accurate results for our EC-MOF systems, as discussed in greater detail in our recent work.¹⁸ The first stage of our HTS workflow is to geometrically relax all structures obtained from CrySP to find the ground-state energy configurations for both the ions and electrons. The criteria for optimization convergence is set to $<10^{-4}$ eV for electronic energy, and the magnitude of the largest force acting on the atoms is set to <0.02 eV/Å. Three degrees of freedom are allowed to change: atomic positions,

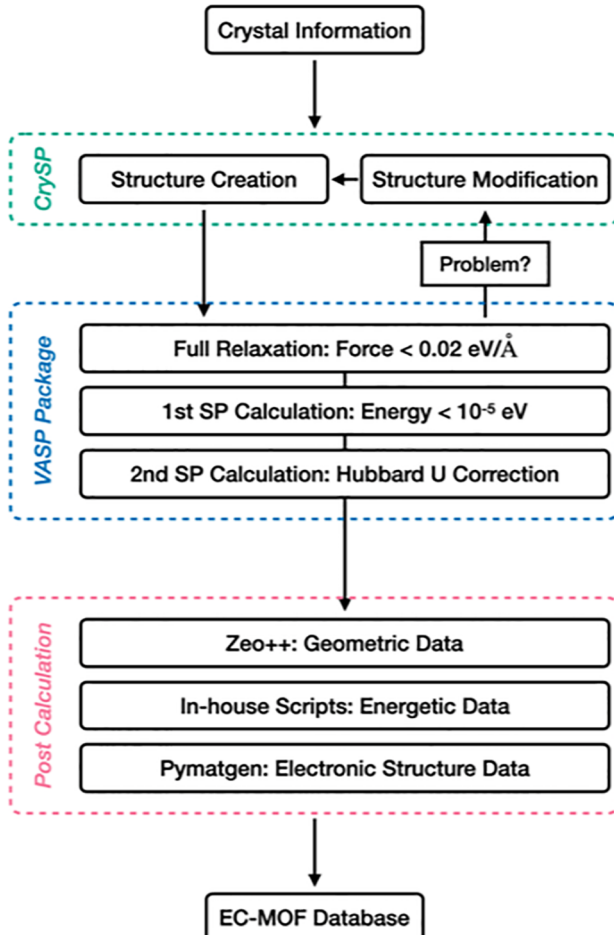


Figure 4. High-throughput screening workflow employed in this work including different steps of geometric relaxations and single-point energy calculations for all structures included in the EC-MOF/Phase-I database.

cell volume, and cell shape for all bulk systems. Cell volume is fixed during the optimization of the monolayers because we use a slab model with *c* = 20 Å to prevent interaction between layers from different periodic cells. If the optimization encounters structure and setting-related issues or has any difficulty in reaching convergence, an automatic debugging process is executed to collect error messages, which automatically updates the input files for reoptimization. Once the optimization is completed, the first round of single-point (SP) calculations is carried out to check if there are any structural or setting-related issues and to provide a good initial electron density for the following calculations. The convergence criteria for electronic energy is set to 1×10^{-5} eV. The Brillouin zones are sampled using $2 \times 2 \times 6$ or $2 \times 2 \times 4$ k-point mesh for bulk systems depending on different ratios of cell parameters and $3 \times 3 \times 1$ k-point mesh for all monolayer systems. The Gaussian smearing method, with a smearing width of 0.05 eV, is adopted in this step to provide accurate electronic energy and density information. The second round of SP calculations reads the electron density calculated in the first round, which increases efficiency. The smearing method is changed to the tetrahedron method with Blöchl corrections, which provides more accurate results for the calculated band gaps and density of states (DOS).⁴⁹ DFT in its GGA formalism is known for underestimating band gaps. Hence, the Hubbard *U* approach (DFT

$+U$), which semiempirically optimizes the Coulomb interaction potential (U), is adopted in this step to give a better description of electronic structures. Only d and f electrons were treated by this approach with the employed semiempirical U parameters for each metal reported in the Supporting Information, section S2 and Table S1. To validate the accuracy of our calculated band gaps, the computed values obtained at the PBE-D3 level with the U correction were benchmarked against the HLE17 meta-GGA functional as implemented in the Minnesota VASP Functional Module codes, and it is already shown to provide band gap values for different materials that are in good agreement with experimental results.^{50,51} For this benchmark, we have chosen semiconductors with the highest band gap values among both bulk and monolayer systems. The results in Figure 5 show that

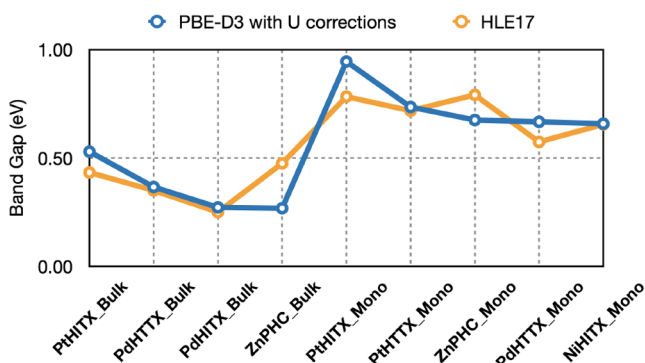


Figure 5. Calculated band gap values for selected semiconductors from the EC-MOF/Phase-I database. The results from DFT+ U and HLE17 functionals are shown in blue and orange, respectively.

DFT+ U qualitatively reproduces the same trend as HLE17 data. Accordingly, the successful completion of both SP steps provided the necessary information for us to extract the final property data from our EC-MOF/Phase-I database.

2.4. Post-Calculation Analysis. Our HTS calculations provide us with different properties including geometric, energetic, and electronic data for all structures generated and contained in our EC-MOF/Phase-I database. Periodic crystal structures are extracted as CIF files after the geometry optimization stage. Analysis of the Voronoi network, as implemented in Zeo++,⁵² is used to determine different geometric data including largest cavity diameter (LCD), accessible void-volume fraction, and accessible surface area, using a helium probe with a radius of 1.4 Å, for all bulk EC-MOFs. From SP calculations, the total energy and electronic structures of the systems are obtained. The absolute formation energy, which is an important indicator of the stabilities of different structures, is calculated as⁵³

$$E_f = E_{\text{tot}} - \frac{1}{N} \sum_{i=1}^N x_i \mu_i \quad (1)$$

where E_{tot} is the calculated energy for the entire bulk material, N is the total number of atoms, and x_i and μ_i are the number and chemical potential, respectively, of element i in the structure. Calculations of each element in their most stable configuration are implemented to find the energy values per atom, which is needed in eq 1. The calculated chemical potentials for all elements are listed in Table S2. Interlayer binding energies were calculated as follows,⁵⁴

$$E_b = \left(E_M - \frac{1}{n} E_B \right) / A \quad (2)$$

where E_M is the calculated energy of the monolayer, n is the number of layers in the bulk structure, E_B is the calculated energy of the bulk structure, and A is the surface area of the monolayer. All the needed energetic data are extracted and calculated by our in-house codes. Electronic band gaps are obtained from VASP using Python Materials Genomics (Pymatgen).⁵⁵ The band centers of the d orbitals are extracted using Pymatgen and the following equation,⁵⁶

$$C_d = \frac{\int_{-\infty}^{+\infty} \rho E dE}{\int_{-\infty}^{+\infty} \rho dE} \quad (3)$$

where C_d is the position of the d-band center, ρ is the density of the d orbitals, E is the energy of the d orbitals relative to the Fermi level, and ρdE is the number of states contributed by d orbitals.

3. RESULTS AND DISCUSSION

Our database contains 1 063 EC-MOF crystal structures that are fully relaxed using the periodic boundary conditions at the DFT level. A wide range of data including structural information, formation energies, and electronic properties are extracted and included in our EC-MOF/Phase-I database, which can be accessed via <https://ec-mof.njit.edu>. Such data are useful for other researchers who need to screen and target attractive properties without additional effort. Here, we discuss these calculated properties in more detail.

3.1. Structural Data Analysis. After full geometric relaxation, a total number of 535 bulk EC-MOFs are successfully converged to the force criteria outlined earlier except the ZnHTTX_Bulk system. In the case of the monolayer structures, eight MPIC systems failed to maintain their connectivity and topology due to strong steric hindrances. Hence, they were not included in the online EC-MOF/Phase-I database nor here. This results in 1 063 structures in the EC-MOF/Phase-I database. Another notable point about monolayer systems is that the optimized structures of HAT-based MOFs are slightly distorted due to the steric hindrance between two neighboring organic linkers. Similar phenomena were observed by Lyu et al.⁵⁷ where monolayer HAT-based MOFs could only be synthesized by an on-surface reaction approach. Here, we first present structural data extracted from 535 optimized bulk systems. Figure 6a shows the frequency of structures as a function of the largest cavity diameter (LCD), which is defined as the diameter of a sphere that can fit into the largest pore of the material.⁵² The LCDs of 2D MOFs in our EC-MOF database range from 0 to 25.2 Å depending on the size of the organic linkers. Structures with the highest LCD values consist of TC-, HATN-, and TN-based MOFs with the largest linker sizes of all. Structures with small LCD values are mostly C-based MOFs. The high number of connectivities of one C linker to the metal nodes limits the spatial space, leading to an LCD value of 0 Å. It should be noted that the computed 0 value for LCD does not mean that the system is not porous but rather that the diameter of the helium probe is larger than the diameter of the pore in these structures. The calculated LCDs of the rest of the structures are qualitatively ranked according to the size of their organic linkers. PC- and PCM-based MOFs, where linkers have similar sizes, constitute a large

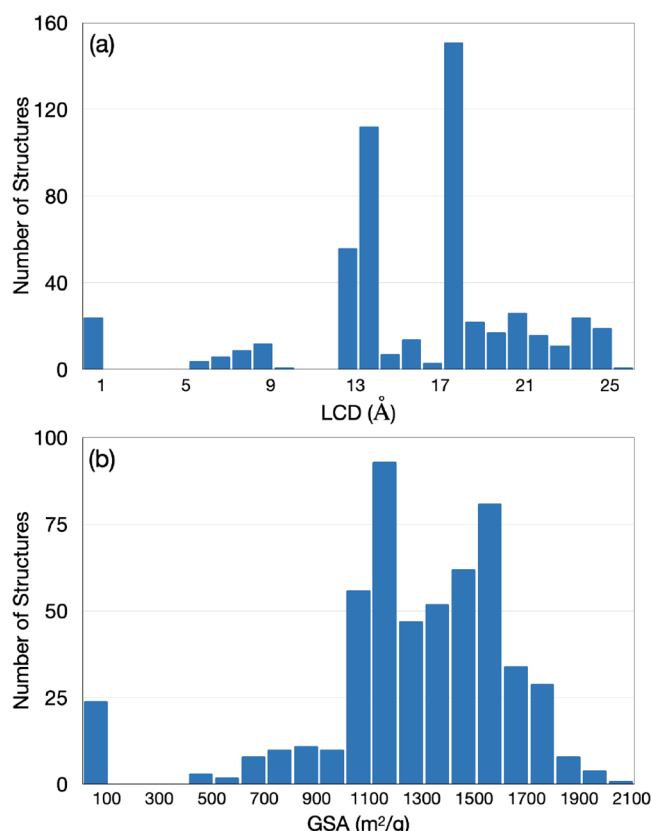


Figure 6. Number of structures from our EC-MOF database as a function of the calculated (a) largest cavity diameters (LCDs) and (b) gravimetric surface areas (GSAs).

body of MOFs with LCDs of $\sim 13 \text{ \AA}$ (Figure 6a). Similarly, NPc- and NPcM-based MOFs constitute the peak at $\sim 17 \text{ \AA}$ in Figure 6a. Figure 6b shows the frequency of structures as a function of gravimetric surface area (GSA). In the range above $1700 \text{ m}^2/\text{g}$, TC, HATN, TN, and TX linkers along with several tetragonal linkers take the lead as the MOFs with the largest GSA values. Due to the unique structures of the TC linkers, TC-based MOFs not only have the conventional 1D channels but also another 1D channel with a smaller radius inside the linkers themselves. Therefore, TC-based MOFs possess the highest GSA with an average value of $1711 \text{ m}^2/\text{g}$ over all combinations of metals and functional groups, as reported in Table 1. Similar results were reported in the work by Park and co-workers,⁵⁸ where CuHHTC was synthesized and featured as a special 2D MOF with an enhanced surface area. In their experimental work, an unprecedentedly high GSA of up to $1196 \text{ m}^2/\text{g}$ was measured that can be compared to CuHHTC in our EC-MOF database with a GSA of $1737 \text{ m}^2/\text{g}$. The GSA of TT-based 2D MOFs was also reported by Dinca and co-workers,⁵⁹ where the GSA of the synthesized CuHHTT is $\sim 1360 \pm 20 \text{ m}^2/\text{g}$ compared to a value of $1549 \text{ m}^2/\text{g}$ calculated in this work. According to our average calculated GSA data, TT-based 2D MOFs rank in fifth place, as shown in Table 1. The structures found in the lowest range of GSA, i.e., $< 500 \text{ m}^2/\text{g}$, are mainly C- and HAT-based MOFs due to the specific connection of the organic linkers and metal nodes in these MOFs and the size of the probe used in Zeo+++. The practical implication of these small cavities will be the adsorptive separation of smaller-sized guest molecules for applications as molecular sieves. When comparing the GSA

Table 1. Average Largest Cavity Diameter and Gravimetric Surface Area Values with Respect to Each Organic Linker

linker	LCD (Å)	GSA (m^2/g)
TC	21.359	1711
HATN	23.800	1639
TN	23.908	1589
TX	20.444	1547
TT	19.737	1502
NPc	17.637	1438
NPcM	17.659	1434
TP	15.381	1201
Pc	12.962	1120
PcM	12.990	1105
B	7.866	663
HAT	5.911	313
C	0	0

data in our EC-MOF database with those from experimentally measured surface areas, our calculated GSA values are always higher than what is measured experimentally by Brunauer–Emmett–Teller (BET) equations. The discrepancy can be mainly related to (1) the size of the crystal particles compared to perfect bulk crystals in our EC-MOF database, (2) the presence of defects in synthesized materials, and (3) pores that are not completely evacuated from solvent molecules. Our calculated GSA data, therefore, provide the maximum surface area that each EC-MOF can possibly reach regardless of the synthesis and activation procedure. Notably, the GSA data in our EC-MOF database show qualitatively similar trends with available experimental results. To reveal the relation between spatial space and accessible surface area, we converted GSA to volumetric surface area (VSA) and plotted them against the void fraction of 13 different organic linkers, as shown in Figure 7. Data points for each linker are highlighted by distinct colors

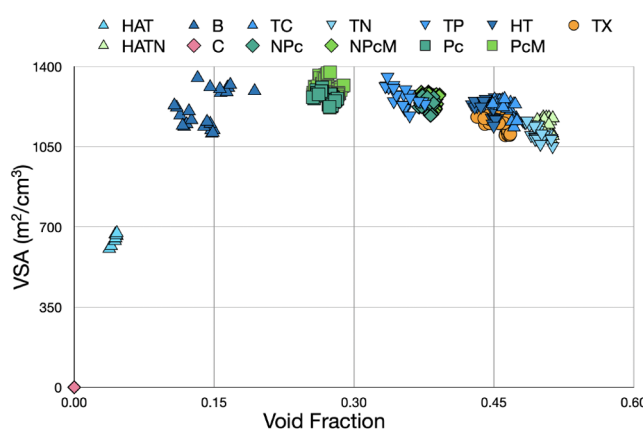


Figure 7. Calculated volumetric surface areas (VSAs) as a function of void fraction according to different organic linkers.

and shapes. In agreement with our GSA data, MOFs containing TN, HATN, TC, TX, and TT linkers possess high void fractions ranging from 0.43 to 0.51 due to the size of the linkers. The data points located between 0.1 and 0.4 void fraction also have high VSA values. However, the difference between VSA values of MOFs with different linkers in this region is less noticeable compared to the difference in their GSA values, as shown in Table 1, due to the inclusion of the density of MOFs in converting GSA to VSA. The void

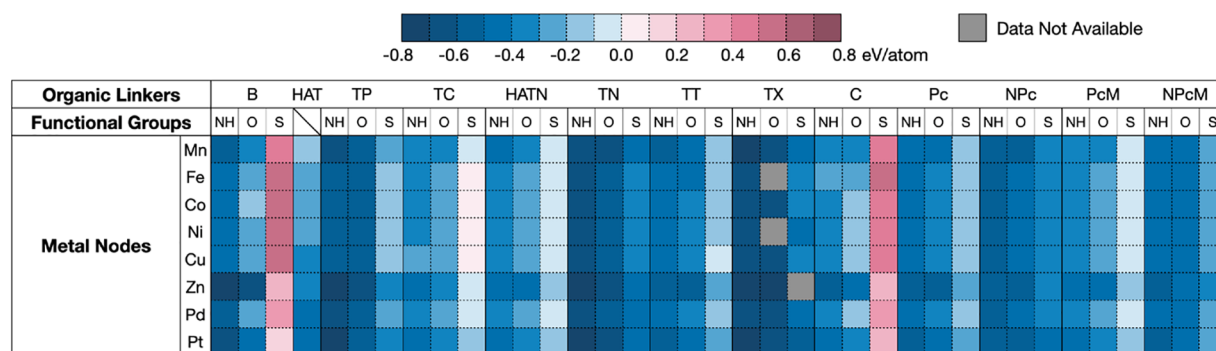


Figure 8. Calculated formation energies (E_f) of all bulk structures contained in our EC-MOF/Phase-I database. The corresponding data for the monolayers are given in Figure S3.

fractions of MOFs with C and HAT linkers are as low as 0.07. Except for these two classes, the VSAs of the rest of the structures are all $>1000 \text{ m}^2/\text{cm}^3$, while their void fractions range all the way from 0.1 to 0.5. Hence, regardless of accessible surface areas, the appropriate MOFs for adsorption/separation applications should be chosen based on the void fraction as well. For energy/gas storage purposes, on the other hand, the gravimetric/volumetric capacities of the active compounds are more relevant.^{60,61} However, applications of these MOFs in adsorption should be further investigated by analyzing the host–guest interactions. For instance, maximizing the performance of MOFs in hydrogen storage requires maximizing VSA while preserving a large void fraction.⁶⁰ On the other hand, the number of adsorption sites should be the primary concern in the case of chemical adsorption.⁶² Here, as an effective descriptor for the host–guest interactions, the d-band center model is integrated into our EC-MOF database, which is further discussed in section 3.4.

3.2. Thermodynamic Data Analysis. Formation energy (E_f) is one of the principal parameters to consider when determining whether a hypothetical material will be synthesizable.^{63,64} Following our high-throughput workflow, calculations of E_f for 1 063 structures were implemented using eq 1, with the results for bulk EC-MOFs presented in Figure 8. Two bulk and four monolayer structures failed to reach the energy convergence during this stage, which decreased the total number of structures in our EC-MOF/Phase-I database to 1 057. Calculated E_f values for the monolayer structures, which show a similar trend to those of the bulk structures, can be found in Figure S2. Both Pcm- and NPcm-based MOFs, which share the same structural building blocks but with different metal centers inside the organic linkers, are combined into one data point. This is because the different choices of metal centers were found to have a minor effect on the calculated E_f values, i.e., $<0.09 \text{ eV/atom}$. Detailed comparisons of these MOFs can be found in Tables S3 and S4. Data points with a blue color in Figure 8 mean negative E_f values and show that the corresponding structures are more likely to be synthesizable. The red-colored data points, on the contrary, correspond to positive E_f values and hence structures that are thermodynamically unstable. Accordingly, 96.06% of the bulk and 92.75% of the monolayer structures have negative E_f values (see Figure 8 and Figure S2). To find a trend in the computed E_f values, one should pay attention to the different bonding/interaction motifs that exist in the built MOFs. Overall, in all EC-MOFs there are three main types of bonds/interactions including covalent bonding within the organic motif,

coordinative bonding between metals and functional groups of the linkers, and comparatively weaker van der Waals interactions between layers. As an example, B, TP, and TN linkers could be placed in an incremental sequence considering that each linker is composed of the previous one plus three more benzene rings. Having more benzene rings in the structure increases the number of covalent bonds, which are stronger than the other two interactions/bond types. Hence, the calculated E_f values of TN-based MOFs are more negative than their TP-based counterparts, which in turn are more stable than the B-based MOFs, all due to the higher number of covalent bonds. A similar trend can also be observed in the cases of Pcm versus NPcm or Pcm versus NPcm, where the latter ones have four more benzene rings than the former ones. Figure 8 also illustrates the E_f values with respect to three functional groups within each linker family. It is very clear that, in each linker family, EC-MOFs with –NH functional groups always possess the most negative formation energies, whereas the ones with –S groups possess the least negative or in some cases even positive values. The stability of the coordinative bonds between transition metals and different functional groups is determined by the compatibility between the two interacting units. Nitrogen atoms have lower electronegativity than oxygen, leading to a stronger bonding to metals. Compared to sulfur atoms, the sizes of nitrogen and oxygen atoms are more similar to that of carbon atoms, which induces a better overlap between atomic orbitals in the extended π -conjugated layers. Considering different transition metals, among eight employed metal nodes, Mn²⁺, Zn²⁺, and Pt²⁺-containing MOFs tend to have more negative E_f values regardless of the organic linker and/or functional group types. Half-filled and fully-filled electronic configurations of Mn²⁺ and Zn²⁺, respectively, are more stable in the same row of the periodic table when forming 2+ ions.

Other than the standard method of creation of MOFs from different building blocks, the physical and chemical properties of the EC-MOF-based layered materials can be further modulated by tuning their interlayer interactions by reducing the number of stacked layers all the way down to a monolayer. Consequently, monolayer materials exfoliated from their corresponding bulk systems may possess unconventional properties in the fields of gas adsorption,⁶⁵ optics,⁶⁶ and electrocatalysis.⁶⁷ EC-MOF monolayers can be synthesized through top-down or bottom-up approaches. Chemical exfoliation methods such as intercalation and electrochemical exfoliation are among the most common techniques in the top-down strategy.⁶⁶ On the contrary, the bottom-up approach is a

more efficient and convenient approach to build monolayer materials by choosing ideal precursors, modulators, and surfactants.⁶⁷ To shed light on the possibility of reaching a monolayer EC-MOF, we have calculated the interlayer binding energies (E_b) according to eq 2 for all structures gathered in our EC-MOF/Phase-I database. Figure 9 shows the histogram

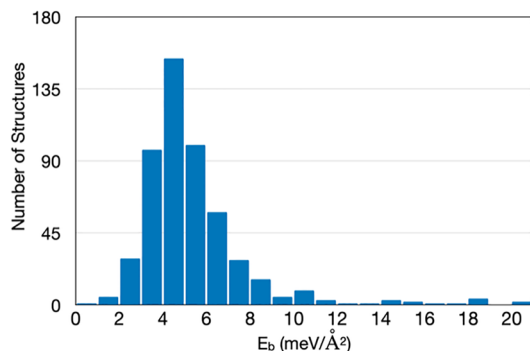


Figure 9. Distribution of structures according to their calculated interlayer binding energies.

for the distribution of all calculated E_b values with a prominent range of 0–20 meV/Å² and a bin width of 1 meV/Å². The E_b values of the majority of our EC-MOFs lie in the range of 2–9 meV/Å². This can be compared to the interlayer binding and exfoliation energies for a large number of layered compounds, including graphite and MoS₂, which are ~20 meV/Å² and have been considered before for successful exfoliations.⁶⁸ It should be mentioned that the low E_b values of the EC-MOFs in comparison to other layered materials relate to the high porosity of our structures. This indicates the promising potential of most of these EC-MOFs for thin-film fabrication, which is of utmost importance in compact device implementations. It is also worthwhile noting that, according to eq 2, calculated E_b values are inversely proportional to the surface area of the monolayer. Hence, within the same family of porous materials, one will naturally obtain smaller E_b values for the systems with larger pore sizes, given similar interlayer van der Waals interactions. For example, EC-MOFs with calculated E_b values >13 meV/Å² are mainly HAT- and C-based MOFs with possibly strong π – π interactions per unit area. To be noted, two structures, MnHAT and PtHHTP, show E_b values higher than 20, 23.17, and 21.57 meV/Å², respectively.

3.3. Electronic Property Data Analysis. The electrically conductive behavior of π -stacked layered MOFs is in contrast to other conventional MOFs that are mostly classified as insulators with highly localized electrons.⁶⁹ To provide more insights into the electrically conductive behavior of the structures gathered in our EC-MOF database, we have calculated their fundamental band gaps as explained in section 2. As a result, 48.59% of the bulk EC-MOFs are calculated to be metallic compared to 31.49% for monolayers (Figure 10). This can be explained by the absence of the interlayer charge transport pathway along the stacking direction for the monolayer structures. We also calculated the ratio of semiconductors within each class of EC-MOFs with different organic linkers (see Table S5) and found that, for most structures, the ratio of semiconductors in monolayers are indeed higher than the ratios in the corresponding bulk systems. Figure S3 shows the nature of conductive behaviors, and band gap values if any, of all structures in the EC-MOF/

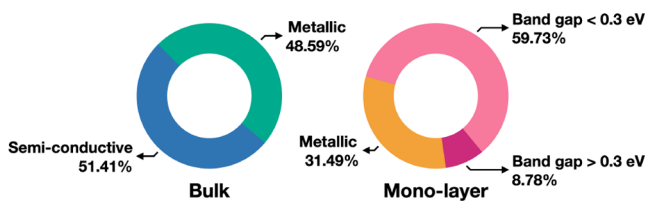


Figure 10. Distribution of the metallic and semiconductor systems in bulk (left) and monolayer (right) materials. Monolayer semiconductors are further divided into two regions according to their band gap values. Detailed band gap data of each structure in the EC-MOF Database can be found in Figure S3.

Phase-I database. A total of 424 structures are found to be metallic, with 259 of them being bulk and the remaining 165 being monolayer systems. For the semiconductors, the maximum band gap value of 0.95 eV is reached by PtHITX_Mono. In Figure S3a, we find that most bulk materials are metallic or narrow-gap semiconductors where the band gap can be <0.15 eV. A maximum band gap of 0.53 eV is recorded for PtHITX_Bulk. In comparison, only one-tenth (~20,00) of structures in the curated 1D MOF collection reported by Gharagheizi et al.²⁷ are metallic, while another one-tenth show a band gap below 1 eV. Furthermore, 546 1D MOFs are insulators (band gap >4 eV), while the band gaps of most structures are in the range of 1–4 eV. It should be again emphasized that, apart from dimensionality that overall affects the properties of MOFs, this difference is related to the fact that we intentionally built our EC-MOF/Phase-I database with structural features that induce a high degree of electrical conductivity in the resulting MOFs. According to our previous work,¹⁸ a transition of conductive behavior between metallic and semiconductor can be easily induced by temperature, pressure, or solvent because of the intrinsic flexibility of these materials. Therefore, such conductive behaviors indicate the great advantage of EC-MOFs compared to conventional MOFs. Indeed, some of them have already been proven to be promising candidates for applications in batteries,⁷⁰ photodetectors,⁷¹ and voltammetric detection.⁷² In Figure S3b, not only does the number of semiconductors increase in monolayers but the band gap values also increase, with the highest band gaps being observed for TX linkers. According to Zhao et al.,⁷³ who reported the successful synthesis of the CuHHTX MOF in 2020, the conductivity of CuHHTX shows an Arrhenius-type dependence on the temperature. The dependence is a typical sign of a semiconductor material that is in agreement with our calculated data. The large band gaps computed for the TX-based MOFs can be explained by the disconnection of the π -conjugation in the benzene rings of the TX linker. Therefore, one can hypothesize that interlayer conduction should play a more prominent role in these systems. PHC-based MOFs are another class that shows wide band gaps. They have the highest number of connectivities, 12 hydroxyl groups per linker. As a result, the very electronegative oxygen atoms tend to localize the charge in the C linker, leading to a wider band gap in these systems compared to other systems. Another interesting trend is found in the Pcm- and NPcm-based monolayers with Ni, Cu, Zn, and Pd inside metals. These monolayers with imino functional groups always possess high band gap values because of the presence of the inside metals compared to the corresponding Pcm- and NPcm-based monolayers. However, no trend was found for Fe and Co as inside metals. Therefore, there could be some long-range

interactions at play between different metals and functional groups that need to be further investigated.

3.4. Adsorption Performance Analysis. As stated earlier, the large surface areas and excellent conductivities of EC-MOFs make them outstanding candidate materials for electronics and energy storage materials. They have been experimentally synthesized for electrode materials in sodium,⁷⁴ lithium–sulfur,⁷⁵ and zinc⁷⁶ batteries. Therefore, it is of high interest to provide insights into not only the conductivities of EC-MOFs but also their capabilities of adsorbing different guest molecules relevant to these applications. Such capability is normally specified in terms of adsorption energy (E_{ads}), which is calculated as

$$E_{\text{ads}} = E_{\text{Guest-Host}} - E_{\text{Guest}} - E_{\text{Host}} \quad (4)$$

Here, $E_{\text{Guest-Host}}$ is the total energy of the guest adsorbed systems, E_{Guest} is the energy of the isolated guest molecules in their stable phases, and E_{Host} is the energy of the host adsorbent materials. To obtain E_{ads} values, accurate DFT relaxations of the guest–host systems, which are rather expensive considering the number of studied materials, are required. Also, for each different guest molecule, a separate relaxation of the entire guest–host system is required because there is no universal model for such interactions. The creation of the EC-MOF database provides the foundation for screening hundreds of low-dimensional materials, utilizing appropriate descriptors, for adsorption purposes without expensive DFT relaxations of the guest–host systems. For example, in the case of transition metals as adsorption sites, the d-band centers of metals can provide some preliminary insights into guest–host interactions without carrying out expensive calculations.⁵⁶ The position of the d-band center is shown to be inversely related to the computed E_{ads} in many studies on metal alloys and also 2D MOFs.^{77,78} More specifically, as the energy of the d-band center increases with respect to the Fermi level, the stronger the interactions become between the guests and the host materials.⁷⁹ The distribution of the d-band centers of bulk and monolayer structures in the EC-MOF Database, except Pcm- and NPcm linker-based MOFs, is demonstrated in Figure 11. Here, we present an exemplary case

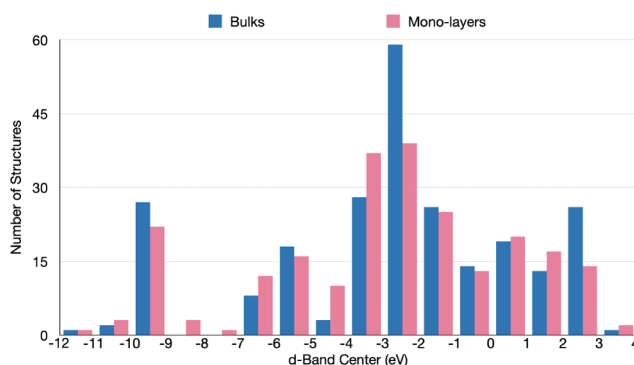


Figure 11. Distribution of the d-band center in bulks and monolayers.

of using the d-band center model to estimate the applicability of selected structures from the EC-MOF database as cathode materials in lithium–sulfur batteries (LSBs). The Li₂S molecule as the final product of the discharge process in LSBs is adapted here as the guest molecule. Two classes of well-studied B- and TP-based MOFs, with imine functional groups, are chosen from our EC-MOF database to serve as the

host materials. Compared to the sp^3 hybridization of the hydroxyl and thiol groups, the imine groups with sp^2 hybridization have less effect on the adsorption process because all three p orbitals are forming σ bonds or conjugating with the π framework of the MOF structures. The fully relaxed structures of the MHIB-Li₂S and MHITP-Li₂S systems (M = Mn, Fe, Co, and Ni) are shown in Figure 12. All systems containing Mn²⁺, Fe²⁺, Co²⁺, and Ni²⁺ metal centers show a similar adsorbing behavior where the Li₂S molecule is adsorbed on the top of the metal nodes. Therefore, their adsorption energies should in principle follow the trend for the d-band center model. The calculated adsorption energies as obtained from eq 4 are plotted versus the corresponding d-band center data in Figure 13, where we can see a clear inverse correlation as expected. The calculated length of the metal–S bonds also indicates the same correlation to the adsorption energies. While we use this example as a proof of concept, care should be taken in choosing a proper descriptor for any specific screening purpose. For example, in the case of the other 4 metal nodes (i.e., M = Cu, Zn, Pd, and Pt), the interaction between functional groups of the MOF and Li atoms of the Li₂S was found to be the dominant adsorption interaction (Figure 13i). Thus, the calculated E_{ads} values were found to not correlate with the computed trend for the d-band center model. Similarly, NiHBB shows a strong contribution of hydroxyl groups for Li₂S. On the other hand, the d-band center has been shown to be a very appropriate descriptor to study the adsorption of adsorbates like OH*, O*, and OOH* species in the oxygen reduction reaction,^{80,81} where E_{ads} values are well-correlated with the d-band center as long as the metal centers act as the primary adsorption sites.

4. FUTURE WORK

Our EC-MOF/Phase-I database provides an easily accessible, computationally ready database for π -stacked layered electrically conductive MOFs with diverse information on their structural, electronic, and adsorption properties. We plan to update this database as research in this field grows and expands. It is necessary to update this database in two directions: the diversity of the MOFs included and the types of properties calculated for them. As stated previously, we have elected to restrict the first version of the database according to the structural features that induce the highest electrical conductivity. However, as mentioned before, this is an active area of research, and new organic linkers are introduced almost every day.⁸² Also, MOFs with various topologies, e.g., three-dimensional MOFs, will be included in the future versions of the database.^{83,84} On the basis of our building strategy, permutations of the building blocks will give a comprehensive understanding of these classes of MOFs as well. On the other hand, other relevant properties need to be calculated, such as performance on adsorption/storage of common gas molecules,⁸⁵ partial atomic charges normally used to interpret trends while modeling chemical reactions,⁸⁶ and density of states/band structures, which reveal detailed charge transport pathways. Machine learning techniques have also shown great promise in materials science research for the prediction of formation energies,⁸⁷ adsorption energies,^{88,89} band gap values,²⁵ and designing new materials.⁹⁰ The created crystal structures and their calculated property data gathered in our EC-MOF/Phase-I database provide an ideal data set for applying various machine learning techniques in order to explore their potentials for different applications.

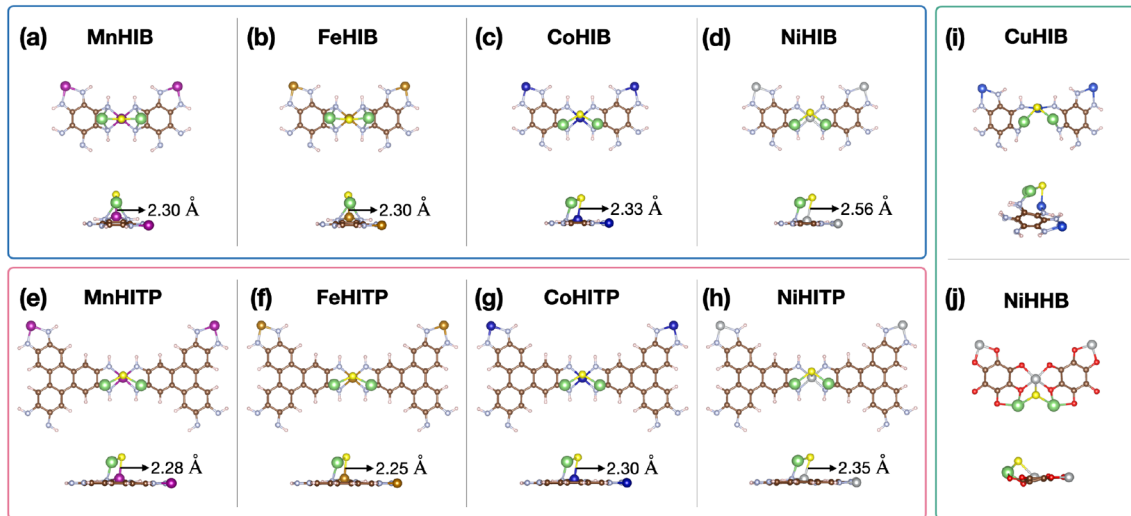


Figure 12. Fully relaxed MHIB (a–d) and MHITP (e–h) MOFs ($M = \text{Mn, Fe, Co, and Ni}$) with Li_2S as the guest molecule. Representative models in different adsorbing behaviors (i, j). In this figure the colors yellow, light blue, red, brown, green, and cream represent sulfur, nitrogen, oxygen, carbon, lithium, and hydrogen atoms, respectively, while metal atoms are distinguishable between different panels.

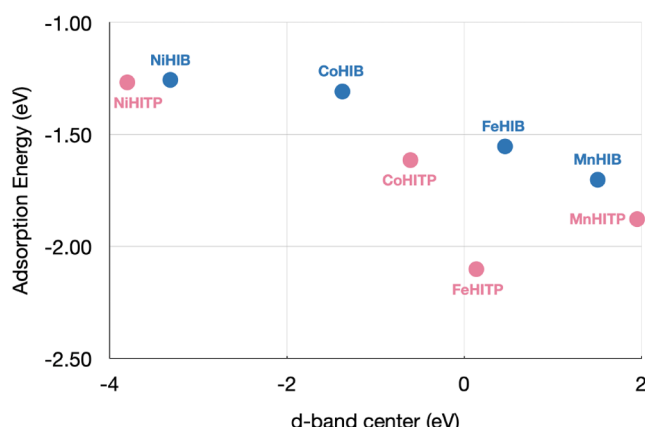


Figure 13. Computed adsorption energies of Li_2S molecules with selected 2D MOF monolayers showing an inverse relation with the corresponding calculated d-band centers.

5. CONCLUSION

In this work, we introduced for the first time an exclusive database for electrically conductive MOFs containing computationally ready structures and their property data. A total of 1,072 structures were created by taking permutations among the subsets of different structural building blocks using our in-house package, Crystal Structure Producer (CrySP). Multiple stages of calculations were applied to the database by applying a high-throughput screening workflow to optimize the structures and calculate their different property data. Of 1,072 structures, 1,063 were successfully optimized at the DFT level, and 1,061 of them successfully completed all stages of calculations, with properties including largest cavity diameter, gravimetric/volumetric surface area, void fraction, formation energy, interlayer binding energy, electronic band gap, and d-band center added into the database. Obtained trends for different classes of MOFs were discussed in great detail, and different materials were classified and analyzed according to their structural or electronic properties, providing comprehen-

The screenshot shows the "Welcome to EC-MOF/Phase-I Database" interface. On the left, there is a "Naming Rule" diagram illustrating the structure of a MOF unit cell: $M_1CXL(M_2)_T$, where M_1 and M_2 are metal nodes, C is an organic linker, X is a functional group, and T indicates the connectivity. Below this are tables for "molecular units" and "packing set". On the right, the main interface displays the crystal structure of FeOIPcCo_Bulk.cif, showing a 3D grid of metal nodes (Fe, Co) and organic linkers (OIPc). Various parameters are listed: $a=18.345\text{\AA}$, $b=18.345\text{\AA}$, $c=22.11\text{\AA}$, $\alpha=90.000^\circ$, $\beta=90.000^\circ$, $\gamma=90.002^\circ$. Below the structure are "DISPLAY OPTIONS" for Spacefill, Ball and Stick, Wireframe, and Switch Background. At the bottom, a table provides detailed properties for FeOIPcCo_Bulk.cif, including MOF Name, Volume, Density, AV_Void Fraction, GSA, VSA, LCD, POAV, E_F (eV), E_B (meV), Band_Gap (eV), Metal_Center, and Links.

MOF Name	Volume (\AA^3)	Density (g/cm^3)	AV_Void Fraction	GSA (m^2/cm^3)	VSA (m^2/cm^3)	LCD (\AA)	POAV_Void Fraction	E_F (eV)	E_B (meV)	Band_Gap (eV)	Metal_Center	Links
FeOIPcCo_Bulk	2433.860	1.085	0.269	1191.250	1262.610	12.370	0.449	-0.3514	6.8811	0.0460	Fe	OIPcCo

Figure 14. Screenshot of the web-based graphical user interface developed for the EC-MOF/Phase-I database available at [https://ec-mof.njt.edu](https://ec-mof.njit.edu).

sive and important information on different families of EC-MOFs. Also, a limited-scale screening of the adsorption performance of the Li₂S molecule was implemented to indicate the possibility of using the d-band center model as an efficient energy descriptor for adsorption energies. Finally, an exclusive graphical user interface (**Figure 14**) was developed and released, at <https://ec-mof.njit.edu>, for this database where all curated structures at the DFT level can be visualized and downloaded with their relevant calculated properties tabulated.

■ ASSOCIATED CONTENT

SI Supporting Information

The Supporting Information is available free of charge at <https://pubs.acs.org/doi/10.1021/acsami.2c22665>.

Mathematical equations for the calculation of cell parameters in CrySP, Hubbard U parameters used in this work, chemical potentials calculated in VASP using the most stable configurations of the pure elements, calculated formation energies, and computed ratios of semiconductor materials to the total number of structures divided between different organic linkers ([PDF](#))

■ AUTHOR INFORMATION

Corresponding Authors

Mohammad R. Momeni — *Division of Energy, Matter and Systems, School of Science and Engineering, University of Missouri—Kansas City, Kansas City, Missouri 64110, United States;* [ORCID iD](https://orcid.org/0000-0002-7731-5823); Email: mmomenitaheri@umkc.edu

Farnaz A. Shakib — *Department of Chemistry and Environmental Science, New Jersey Institute of Technology, Newark, New Jersey 07102, United States;* [ORCID iD](https://orcid.org/0000-0003-1432-2812); Email: shakib@njit.edu

Authors

Zeyu Zhang — *Department of Chemistry and Environmental Science, New Jersey Institute of Technology, Newark, New Jersey 07102, United States*

Dylan S. Valente — *Department of Chemistry and Environmental Science, New Jersey Institute of Technology, Newark, New Jersey 07102, United States*

Yuliang Shi — *Department of Chemistry and Environmental Science, New Jersey Institute of Technology, Newark, New Jersey 07102, United States*

Dil K. Limbu — *Department of Chemistry and Environmental Science, New Jersey Institute of Technology, Newark, New Jersey 07102, United States;* [ORCID iD](https://orcid.org/0000-0001-9196-9498)

Complete contact information is available at:

<https://pubs.acs.org/10.1021/acsami.2c22665>

Notes

The authors declare no competing financial interest.

■ ACKNOWLEDGMENTS

F.A.S. acknowledges support from the New Jersey Institute of Technology (NJIT). This work used Bridges2 at Pittsburgh Supercomputing Center through allocation CHE200007 from the Extreme Science and Engineering Discovery Environment (XSEDE),⁹¹ which was supported by National Science Foundation Grant no. 1548562. This research has been

(partially) enabled by the use of computing resources and technical support provided by the HPC center at NJIT.

■ REFERENCES

- Kitagawa, S.; Kaskel, S.; Xu, Q. Metal-Organic Frameworks: Synthesis, Structures, and Applications. *Small Struct.* **2022**, *3*, 2200072.
- Morris, R. E.; Wheatley, P. S. Gas Storage in Nanoporous Materials. *Angew. Chem., Int. Ed.* **2008**, *47*, 4966–4981.
- Li, J.-R.; Sculley, J.; Zhou, H.-C. Metal-Organic Frameworks for Separations. *Chem. Rev.* **2012**, *112*, 869–932.
- Lee, J.; Farha, O. K.; Roberts, J.; Scheidt, K. A.; Nguyen, S. T.; Hupp, J. T. Metal-Organic Framework Materials as Catalysts. *Chem. Soc. Rev.* **2009**, *38*, 1450–1459.
- Liu, J.; Yin, H.; Liu, P.; Chen, S.; Yin, S.; Wang, W.; Zhao, H.; Wang, Y. Theoretical Understanding of Electrocatalytic Hydrogen Production Performance by Low-Dimensional Metal-Organic Frameworks on the Basis of Resonant Charge-Transfer Mechanisms. *J. Phys. Chem. Lett.* **2019**, *10*, 6955–6961.
- Liu, J.; Hinsch, J. J.; Yin, H.; Liu, P.; Zhao, H.; Wang, Y. Low-Dimensional Metal-Organic Frameworks with High Activity and Selectivity toward Electrocatalytic Chlorine Evolution Reactions. *J. Phys. Chem. C* **2022**, *126*, 7066–7075.
- Furukawa, H.; Cordova, K. E.; O'Keeffe, M.; Yaghi, O. M. The Chemistry and Applications of Metal-Organic Frameworks. *Science* **2013**, *341*, 1230444.
- Yaghi, O. M. Reticular Chemistry in All Dimensions. *ACS Cent. Sci.* **2019**, *5*, 1295–1300.
- Yaghi, O. M.; O'Keeffe, M.; Ockwig, N. W.; Chae, H. K.; Eddaoudi, M.; Kim, J. R. Reticular Synthesis and the Design of New Materials. *Nature* **2003**, *423*, 705–714.
- Groom, C. R.; Bruno, I. J.; Lightfoot, M. P.; Ward, S. C. The Cambridge Structural Database. *Acta. Crystallogr. B. Struct. Sci. Cryst. Eng. Mater.* **2016**, *72*, 171–179.
- Wang, M.; Dong, R.; Feng, X. Two-Dimensional Conjugated Metal-Organic Frameworks (2D c-MOFs): Chemistry and Function for MOFtronics. *Chem. Soc. Rev.* **2021**, *50*, 2764–2793.
- Hmadeh, M.; Lu, Z.; Liu, Z.; Gándara, F.; Furukawa, H.; Wan, S.; Augustyn, V.; Chang, R.; Liao, L.; Zhou, F.; Perre, E.; Ozolins, V.; Suenaga, K.; Duan, X.; Dunn, B.; Yamamoto, Y.; Terasaki, O.; Yaghi, O. M. New porous crystals of extended metal-catecholates. *Chem. Mater.* **2012**, *24*, 3511–3513.
- Wu, G.; Huang, J.; Zang, Y.; He, J.; Xu, G. Porous Field-Effect Transistors Based on a Semiconductive Metal-Organic Framework. *J. Am. Chem. Soc.* **2017**, *139*, 1360–1363.
- Li, W.-H.; Ding, K.; Tian, H.-R.; Yao, M.-S.; Nath, B.; Deng, W.-H.; Wang, Y.; Xu, G. Conductive Metal-Organic Framework Nanowire Array Electrodes for High-Performance Solid-State Supercapacitors. *Adv. Funct. Mater.* **2017**, *27*, 1702067.
- Huang, X.; Zhang, S.; Liu, L.; Yu, L.; Chen, G.; Xu, W.; Zhu, D. Superconductivity in a Copper(II)-Based Coordination Polymer with Perfect Kagome Structure. *Angew. Chem., Int. Ed.* **2018**, *57*, 146–150.
- Dong, R.; Zhang, Z.; Tranca, D. C.; Zhou, S.; Wang, M.; Adler, P.; Liao, Z.; Liu, F.; Sun, Y.; Shi, W.; Zhang, Z.; Zschech, E.; Mannsfeld, S. C. B.; Felser, C.; Feng, X. A Coronene-Based Semiconducting Two-Dimensional Metal-Organic Framework with Ferromagnetic Behavior. *Nat. Commun.* **2018**, *9*, 2637.
- Wada, K.; Sakaushi, K.; Sasaki, S.; Nishihara, H. Multielectron-Transfer-Based Rechargeable Energy Storage of Two-Dimensional Coordination Frameworks with Non-Innocent Ligands. *Angew. Chem., Int. Ed.* **2018**, *130*, 9024–9028.
- Zhang, Z.; Dell'Angelo, D.; Momeni, M. R.; Shi, Y.; Shakib, F. A. Metal-to-Semiconductor Transition in Two-Dimensional Metal-Organic Frameworks: An Ab Initio Dynamics Perspective. *ACS Appl. Mater. Interfaces* **2021**, *13*, 25270–25279.
- Rosen, A. S.; Notestein, J. M.; Snurr, R. Q. Identifying Promising Metal-Organic Frameworks for Heterogeneous Catalysis via High-Throughput Periodic Density Functional Theory. *J. Comput. Chem.* **2019**, *40*, 1305–1318.

- (20) Chung, Y. G.; Camp, J.; Haranczyk, M.; Sikora, B. J.; Bury, W.; Krungleviciute, V.; Yildirim, T.; Farha, O. K.; Sholl, D. S.; Snurr, R. Q. Computation-Ready, Experimental Metal-Organic Frameworks: A Tool to Enable High-Throughput Screening of Nanoporous Crystals. *Chem. Mater.* **2014**, *26*, 6185–6192.
- (21) Nazarian, D.; Camp, J. S.; Sholl, D. S. A Comprehensive Set of High-Quality Point Charges for Simulations of Metal-Organic Frameworks. *Chem. Mater.* **2016**, *28*, 785–793.
- (22) Nazarian, D.; Camp, J. S.; Chung, Y. G.; Snurr, R. Q.; Sholl, D. S. Large-Scale Refinement of Metal-Organic Framework Structures Using Density Functional Theory. *Chem. Mater.* **2017**, *29*, 2521–2528.
- (23) Chung, Y. G.; Haldoupis, E.; Bucior, B. J.; Haranczyk, M.; Lee, S.; Zhang, H.; Vogiatzis, K. D.; Milisavljevic, M.; Ling, S.; Camp, J. S.; Slater, B.; Siepmann, J. I.; Sholl, D. S.; Snurr, R. Q. Advances, Updates, and Analytics for the Computation-Ready, Experimental Metal-Organic Framework Database: CoRE MOF 2019. *J. Chem. Eng. Data* **2019**, *64*, 5985–5998.
- (24) Moghadam, P. Z.; Li, A.; Wiggin, S. B.; Tao, A.; Maloney, A. G.; Wood, P. A.; Ward, S. C.; Fairén-Jiménez, D. Development of a Cambridge Structural Database Subset: a Collection of Metal-Organic Frameworks for Past, Present, and Future. *Chem. Mater.* **2017**, *29*, 2618–2625.
- (25) Rosen, A. S.; Iyer, S. M.; Ray, D.; Yao, Z.; Aspuru-Guzik, A.; Gagliardi, L.; Notestein, J. M.; Snurr, R. Q. *Matter* **2021**, *4*, 1578–1597.
- (26) Wilmer, C. E.; Leaf, M.; Lee, C. Y.; Farha, O. K.; Hauser, B. G.; Hupp, J. T.; Snurr, R. Q. Large-Scale Screening of Hypothetical Metal-Organic Frameworks. *Nat. Chem.* **2012**, *4*, 83–89.
- (27) Gharagheizi, F.; Yu, Z.; Sholl, D. S. Curated Collection of More than 20,000 Experimentally Reported One-Dimensional Metal-Organic Frameworks. *ACS Appl. Mater. Interfaces* **2022**, *14*, 42258–42266.
- (28) Sakaida, S.; Otsubo, K.; Sakata, O.; Song, C.; Fujiwara, A.; Takata, M.; Kitagawa, H. Crystalline Coordination Framework Endowed with Dynamic Gate-Opening Behaviour by Being Downscaled to A Thin Film. *Nat. Chem.* **2016**, *8*, 377–383.
- (29) Sakaida, S.; Haraguchi, T.; Otsubo, K.; Sakata, O.; Fujiwara, A.; Kitagawa, H. Fabrication and Structural Characterization of An Ultrathin Film of a Two-Dimensional-Layered Metal-Organic Framework, $\text{Fe}(\text{py})_2[\text{Ni}(\text{CN})_4]$ (py = pyridine). *Inorg. Chem.* **2017**, *56*, 7606–7609.
- (30) Liu, J.; Zhou, Y.; Xie, Z.; Li, Y.; Liu, Y.; Sun, J.; Ma, Y.; Terasaki, O.; Chen, L. Conjugated Copper-Catecholate Framework Electrodes for Efficient Energy Storage. *Angew. Chem., Int. Ed.* **2020**, *59*, 1081–1086.
- (31) Liao, W. M.; Zhang, J. H.; Yin, S. Y.; Lin, H.; Zhang, X.; Wang, J.; Wang, H. P.; Wu, K.; Wang, Z.; Fan, Y. N.; Pan, M.; Su, C. Y. Tailoring Exciton and Excimer Emission in an Exfoliated Ultrathin 2d Metal-Organic Framework. *Nat. Commun.* **2018**, *9*, 2401.
- (32) Foster, J. A.; Henke, S.; Schneemann, A.; Fischer, R. A.; Cheetham, A. K. Liquid Exfoliation of Alkyl-Ether Functionalised Layered Metal-Organic Frameworks to Nanosheets. *Chem. Commun.* **2016**, *52*, 10474–10477.
- (33) Yang, C.; Dong, R.; Wang, M.; Petkov, P. S.; Zhang, Z.; Wang, M.; Han, P.; Ballabio, M.; Bräuninger, S. A.; Liao, Z.; Zhang, J.; Schwotzer, F.; Zschech, E.; Klauss, H.-H.; Cánovas, E.; Kaskel, S.; Bonn, M.; Zhou, S.; Heine, T.; Feng, X. A Semiconducting Layered Metal-Organic Framework Magnet. *Nat. Commun.* **2019**, *10*, 3260.
- (34) Nnaji, N.; Sen, P.; Nyokong, T. Symmetry Effect of Cobalt Phthalocyanines on the Aluminium Corrosion Inhibition in Hydrochloric Acid. *Mater. Lett.* **2022**, *306*, 130892.
- (35) Meng, Z.; Aykanat, A.; Mirica, K. A. Welding Metalphthalocyanines into Bimetallic Molecular Meshes for Ultra-sensitive, Low-Power Chemiresistive Detection of Gases. *J. Am. Chem. Soc.* **2019**, *141*, 2046–2053.
- (36) Wang, M.; Shi, H.; Zhang, P.; Liao, Z.; Wang, M.; Zhong, H.; Schwotzer, F.; Nia, A. S.; Zschech, E.; Zhou, S.; Kaskel, S.; Dong, R.; Feng, X. Phthalocyanine-Based 2D Conjugated Metal-Organic Framework Nanosheets for High-Performance Micro-Supercapacitors. *Adv. Funct. Mater.* **2020**, *30*, 2002664.
- (37) He, X.-h.; Zhao, M.; Tian, X.-y.; Lu, Y.-j.; Yang, S.-y.; Peng, Q.-r.; Yang, M.; Jiang, W.-w. Redox-Responsive Nano-Micelles Containing Trisulfide Bonds to Enhance Photodynamic Efficacy of Zinc Naphthalocyanine. *Chem. Phys. Lett.* **2022**, *803*, 139785.
- (38) Kulu, I.; Mantareva, V.; Kussovski, V.; Angelov, I.; Durmuş, M. Effects of Metal Ion in Cationic Pd (II) and Ni (II) Phthalocyanines on Physicochemical and Photodynamic Inactivation Properties. *J. Mol. Struct.* **2022**, *1247*, 131288.
- (39) Liu, J.; Chen, Y.; Feng, X.; Dong, R. Conductive 2D Conjugated Metal-Organic Framework Thin Films: Synthesis and Functions for (Opto-) Electronics. *Small Struct.* **2022**, *3*, 2100210.
- (40) Ko, M.; Mendecki, L.; Mirica, K. A. Conductive Two-Dimensional Metal-Organic Frameworks as Multifunctional Materials. *Chem. Commun.* **2018**, *54*, 7873–7891.
- (41) Kresse, G.; Hafner, J. Ab initio Molecular Dynamics for Liquid Metals. *Phys. Rev. B* **1993**, *47*, 558–561.
- (42) Kresse, G.; Hafner, J. Ab initio Molecular-Dynamics Simulation of the Liquid-Metal-Amorphous-Semiconductor Transition in Germanium. *Phys. Rev. B* **1994**, *49*, 14251–14269.
- (43) Kresse, G.; Furthmüller, J. Efficiency of Ab-initio Total Energy Calculations for Metals and Semiconductors Using a Plane-Wave Basis Set. *Comput. Mater. Sci.* **1996**, *6*, 15–50.
- (44) Kresse, G.; Furthmüller, J. Efficient Iterative Schemes for Ab initio Total-Energy calculations using a plane-wave basis set. *Phys. Rev. B* **1996**, *54*, 11169–11186.
- (45) Blöchl, P. E. Projector Augmented-Wave Method. *Phys. Rev. B* **1994**, *50*, 17953.
- (46) Kresse, G.; Joubert, D. From Ultrasoft Pseudopotentials to the Projector Augmented-Wave Method. *Phys. Rev. B* **1999**, *59*, 1758.
- (47) Perdew, J. P.; Burke, K.; Ernzerhof, M. Generalized Gradient Approximation Made Simple. *Phys. Rev. Lett.* **1996**, *77*, 3865.
- (48) Grimme, S.; Antony, J.; Ehrlich, S.; Krieg, H. A Consistent and Accurate Ab initio Parametrization of Density Functional Dispersion Correction (DFT-D) for the 94 Elements H-Pu. *Chem. Phys.* **2010**, *132*, 154104.
- (49) Sholl, D. S.; Steckel, J. A. *Density Functional Theory: A Practical Introduction*; John Wiley & Sons: 2011.
- (50) Verma, P.; Truhlar, D. G. HLE17: An Improved Local Exchange-Correlation Functional for Computing Semiconductor Band Gaps and Molecular Excitation Energies. *J. Phys. Chem. C* **2017**, *121*, 7144–7154.
- (51) Choudhuri, I.; Truhlar, D. G. HLE17: An Efficient Way to Predict Band Gaps of Complex Materials. *J. Phys. Chem. C* **2019**, *123*, 17416–17424.
- (52) Willems, T. F.; Rycroft, C. H.; Kazi, M.; Meza, J. C.; Haranczyk, M. Algorithms and Tools for High-Throughput Geometry-Based Analysis of Crystalline Porous Materials. *Microporous Mesoporous Mater.* **2012**, *149*, 134–141.
- (53) Kirklin, S.; Saal, J. E.; Meredig, B.; Thompson, A.; Doak, J. W.; Aykol, M.; Rühl, S.; Wolverton, C. The Open Quantum Materials Database (OQMD): Assessing the Accuracy of DFT Formation Energies. *npj Comput. Mater.* **2015**, *1*, 15010.
- (54) Huang, J.; Golomb, M. J.; Kavanagh, S. R.; Tolborg, K.; Ganose, A. M.; Walsh, A. Band Gap Opening from Displacive Instabilities in Layered Covalent-Organic Frameworks. *J. Mater. Chem. A* **2022**, *10*, 13500–13507.
- (55) Jain, A.; Hautier, G.; Moore, C. J.; Ping Ong, S.; Fischer, C. C.; Mueller, T.; Persson, K. A.; Ceder, G. A High-Throughput Infrastructure for Density Functional Theory Calculations. *Comput. Mater. Sci.* **2011**, *50*, 2295–2310.
- (56) Hammer, B.; Norskov, J. K. Why Gold is the Noblest of All the Metals. *Nature* **1995**, *376*, 238–240.
- (57) Lyu, C.-K.; Gao, Y.-F.; Gao, Z.-A.; Mo, S.-Y.; Hua, M.-Q.; Li, E.; Fu, S.-Q.; Chen, J.-Y.; Liu, P.-N.; Huang, L.; Lin, N. Synthesis of Single-Layer Two-Dimensional Metal-Organic Frameworks $\text{M}_3(\text{HAT})_2$ ($\text{M} = \text{Ni}, \text{Fe}, \text{Co}$, $\text{HAT} = 1, 4, 5, 8, 9, 12$ -

- hexaazatriphenylene) Using an On-Surface Reaction. *Angew. Chem.* **2022**, *134*, e202204528.
- (58) Pham, H. T.; Choi, J. Y.; Huang, S.; Wang, X.; Claman, A.; Stodolka, M.; Yazdi, S.; Sharma, S.; Zhang, W.; Park, J. Imparting Functionality and Enhanced Surface Area to a 2D Electrically Conductive MOF via Macrocyclic Linker. *J. Am. Chem. Soc.* **2022**, *144*, 10615–10621.
- (59) Dou, J.-H.; Arguilla, M. Q.; Luo, Y.; Li, J.; Zhang, W.; Sun, L.; Mancuso, J. L.; Yang, L.; Chen, T.; Parent, L. R.; Skorupskii, G.; Libretto, N. J.; Sun, C.; Yang, M. C.; Dip, P. V.; Brignole, E. J.; Miller, J. T.; Kong, J.; Hendon, C. H.; Sun, J.; Dincă, M. Atomically Precise Single-Crystal Structures of Electrically Conducting 2D Metal-Organic Frameworks. *Nat. Mater.* **2021**, *20*, 222–228.
- (60) Gómez-Gualdrón, D. A.; Wang, T. C.; García-Holley, P.; Saweleta, R. M.; Argueta, E.; Snurr, R. Q.; Hupp, J. T.; Yildirim, T.; Farha, O. K. Understanding Volumetric and Gravimetric Hydrogen Adsorption Trade-Off in Metal-Organic Frameworks. *ACS Appl. Mater. Interfaces* **2017**, *9*, 33419–33428.
- (61) Allendorf, M. D.; Hulvey, Z.; Gennett, T.; Ahmed, A.; Autrey, T.; Camp, J.; Seon Cho, E.; Furukawa, H.; Haranczyk, M.; Head-Gordon, M.; Jeong, S.; Karkamkar, A.; Liu, D.-J.; Long, J. R.; Meihaus, K. R.; Nayyar, I. H.; Nazarov, R.; Siegel, D. J.; Stavila, V.; Urban, J. J.; Veccham, S. P.; Wood, B. C. An Assessment of Strategies for the Development of Solid-State Adsorbents for Vehicular Hydrogen Storage. *Energy Environ. Sci.* **2018**, *11*, 2784–2812.
- (62) Li, F.; Zhang, X.; Liu, X.; Zhao, M. Novel Conductive Metal-Organic Framework for a High-Performance Lithium-Sulfur Battery Host: 2D Cu-Benzenehexathial (BHT). *ACS Appl. Mater. Interfaces* **2018**, *10*, 15012–15020.
- (63) Rasmussen, F. A.; Thygesen, K. S. Computational 2D Materials Database: Electronic Structure of Transition-Metal Dichalcogenides and Oxides. *J. Phys. Chem. C* **2015**, *119*, 13169–13183.
- (64) Mao, Y.; Yang, H.; Sheng, Y.; Wang, J.; Ouyang, R.; Ye, C.; Yang, J.; Zhang, W. Prediction and Classification of Formation Energies of Binary Compounds by Machine Learning: an Approach without Crystal Structure Information. *ACS Omega* **2021**, *6*, 14533–14541.
- (65) Liu, L.-L.; Chen, J.; Zhang, Y.; Yu, C.-X.; Du, W.; Sun, X.-Q.; Zhang, J.-L.; Hu, F.-L.; Mi, Y.; Ma, L.-F. Fabrication of Ultrathin Single-Layer 2D Metal-Organic Framework Nanosheets with Excellent Adsorption Performance via a Facile Exfoliation Approach. *J. Mater. Chem. A* **2021**, *9*, 546–555.
- (66) Zheng, Y.; Sun, F.-Z.; Han, X.; Xu, J.; Bu, X.-H. Recent Progress in 2D Metal-Organic Frameworks for Optical Applications. *Adv. Opt. Mater.* **2020**, *8*, 2000110.
- (67) Khan, U.; Nairan, A.; Gao, J.; Zhang, Q. Current Progress in 2D Metal-Organic Frameworks for Electrocatalysis. *Small Struct.* **2022**, 2200109.
- (68) Björkman, T.; Gulans, A.; Krasheninnikov, A. V.; Nieminen, R. M. van der Waals Bonding in Layered Compounds from Advanced Density-Functional First-Principles Calculations. *Phys. Rev. Lett.* **2012**, *108*, 235502.
- (69) Kung, C.-W.; Han, P.-C.; Chuang, C.-H.; Wu, K. C.-W. Electronically Conductive Metal-Organic Framework-Based Materials. *APL Mater.* **2019**, *7*, 110902.
- (70) Cai, D.; Lu, M.; Li, L.; Cao, J.; Chen, D.; Tu, H.; Li, J.; Han, W. Lithium-Sulfur Batteries: A Highly Conductive MOF of Graphene Analogue $\text{Ni}_3(\text{HITP})_2$ as a Sulfur Host for High-Performance Lithium-Sulfur Batteries. *Small* **2019**, *15*, 1970240.
- (71) Arora, H.; Dong, R.; Venanzi, T.; Zscharschuch, J.; Schneider, H.; Helm, M.; Feng, X.; Cánovas, E.; Erbe, A. Demonstration of a Broadband Photodetector Based on a Two-Dimensional Metal-Organic Framework. *Adv. Mater.* **2020**, *32*, 1907063.
- (72) Ko, M.; Mendecki, L.; Eagleton, A. M.; Durbin, C. G.; Stoltz, R. M.; Meng, Z.; Mirica, K. A. Employing Conductive Metal-Organic Frameworks for Voltammetric Detection of Neurochemicals. *J. Am. Chem. Soc.* **2020**, *142*, 11717–11733.
- (73) Zhao, Q.; Li, S.-H.; Chai, R.-L.; Ren, X.; Zhang, C. Two-Dimensional Conductive Metal-Organic Frameworks Based on Truxene. *ACS Appl. Mater. Interfaces* **2020**, *12*, 7504–7509.
- (74) Park, J.; Lee, M.; Feng, D.; Huang, Z.; Hinckley, A. C.; Yakovenko, A.; Zou, X.; Cui, Y.; Bao, Z. Stabilization of Hexaaminobenzene in a 2D Conductive Metal-Organic Framework for High Power Sodium Storage. *J. Am. Chem. Soc.* **2018**, *140*, 10315–10323.
- (75) Cai, D.; Lu, M.; Li, L.; Cao, J.; Chen, D.; Tu, H.; Li, J.; Han, W. A Highly Conductive MOF of Graphene Analogue $\text{Ni}_3(\text{HITP})_2$ as a Sulfur Host for High-Performance Lithium-Sulfur Batteries. *Small* **2019**, *15*, 1902605.
- (76) Nam, K. W.; Park, S. S.; Dos Reis, R.; Dravid, V. P.; Kim, H.; Mirkin, C. A.; Stoddart, J. F. Conductive 2D Metal-Organic Framework for High-Performance Cathodes in Aqueous Rechargeable Zinc Batteries. *Nat. Commun.* **2019**, *10*, 4948.
- (77) Zeng, P.; Liu, C.; Cheng, C.; Yuan, C.; Dai, K.; Mao, J.; Zheng, L.; Zhang, J.; Chang, L.-Y.; Haw, S.-C.; Chan, T.-S.; Lin, H.; Zhang, L. Propelling Polysulfide Redox Conversion by d-Band Modulation for High Sulfur Loading and Low Temperature Lithium-Sulfur Batteries. *J. Mater. Chem. A* **2021**, *9*, 18526–18536.
- (78) Li, T.; He, C.; Zhang, W. Two-Dimensional Porous Transition Metal Organic Framework Materials with Strongly Anchoring Ability as Lithium-Sulfur Cathode. *Energy Storage Mater.* **2020**, *25*, 866–875.
- (79) Nørskov, J. K.; Bligaard, T.; Rossmeisl, J.; Christensen, C. H. Towards the Computational Design of Solid Catalysts. *Nat. Chem.* **2009**, *1*, 37–46.
- (80) Gao, G.; Waclawik, E. R.; Du, A. Computational Screening of Two-Dimensional Coordination Polymers as Efficient Catalysts for Oxygen Evolution and Reduction Reaction. *J. Catal.* **2017**, *352*, 579–585.
- (81) Zhou, J.; Han, Z.; Wang, X.; Gai, H.; Chen, Z.; Guo, T.; Hou, X.; Xu, L.; Hu, X.; Huang, M.; Levchenko, S. V.; Jiang, H. Discovery of Quantitative Electronic Structure-OER Activity Relationship in Metal-Organic Framework Electrocatalysts Using an Integrated Theoretical-Experimental Approach. *Adv. Funct. Mater.* **2021**, *31*, 2102066.
- (82) Guo, B.; Xu, R.; Liang, J.; Zou, L.; Terfort, A.; Tian, Z.; Liu, P.; Wang, T.; Liu, J. Dialytic Synthesis of Two-Dimensional Cu-Based Metal-Organic Frameworks for Gas Separation: Designable MOF-Polymer Interface. *Inorg. Chem.* **2022**, *61*, 16197–16202.
- (83) Sun, L.; Hendon, C. H.; Park, S. S.; Tulchinsky, Y.; Wan, R.; Wang, F.; Walsh, A.; Dincă, M. Is Iron Unique in Promoting Electrical Conductivity in MOFs? *Chem. Sci.* **2017**, *8*, 4450–4457.
- (84) Darago, L. E.; Aubrey, M. L.; Yu, C. J.; Gonzalez, M. I.; Long, J. R. Electronic Conductivity, Ferrimagnetic Ordering, and Reductive Insertion Mediated by Organic Mixed-Valence in a Ferric Semiquinoid Metal-Organic Framework. *J. Am. Chem. Soc.* **2015**, *137*, 15703–15711.
- (85) Colón, Y. J.; Gomez-Gualdrón, D. A.; Snurr, R. Q. Topologically Guided, Automated Construction of Metal-Organic Frameworks and Their Evaluation for Energy-Related Applications. *Cryst. Growth Des.* **2017**, *17*, 5801–5810.
- (86) Rosen, A. S.; Fung, V.; Huck, P.; O'Donnell, C. T.; Horton, M. K.; Truhlar, D. G.; Persson, K. A.; Notestein, J. M.; Snurr, R. Q. High-Throughput Predictions of Metal–Organic Framework Electronic Properties: Theoretical Challenges, Graph Neural Networks, and Data Exploration. *Npj Comput. Mater.* **2022**, *8*, 112.
- (87) Gong, S.; Wang, S.; Xie, T.; Chae, W. H.; Liu, R.; Shao-Horn, Y.; Grossman, J. C. Calibrating DFT Formation Enthalpy Calculations by Multifidelity Machine Learning. *JACS Au* **2022**, *2*, 1964–1977.
- (88) Panapitiya, G.; Avendaño-Franco, G.; Ren, P.; Wen, X.; Li, Y.; Lewis, J. P. Machine-Learning Prediction of CO Adsorption in Thiolated, Ag-Alloyed Au Nanoclusters. *J. Am. Chem. Soc.* **2018**, *140*, 17508–17514.
- (89) Wang, X.; Ye, S.; Hu, W.; Sharman, E.; Liu, R.; Liu, Y.; Luo, Y.; Jiang, J. Electric Dipole Descriptor for Machine Learning Prediction of Catalyst Surface-Molecular Adsorbate Interactions. *J. Am. Chem. Soc.* **2020**, *142*, 7737–7743.

- (90) Mai, H.; Le, T. C.; Chen, D.; Winkler, D. A.; Caruso, R. A. Machine Learning for Electrocatalyst and Photocatalyst Design and Discovery. *Chem. Rev.* **2022**, *122*, 13478–13515.
- (91) Towns, J.; Cockerill, T.; Dahan, M.; Foster, I.; Gaither, K.; Grimshaw, A.; Hazlewood, V.; Lathrop, S.; Lifka, D.; Peterson, G. D.; Roskies, R.; Scott, J. R.; Wilkins-Diehr, N. XSEDE: Accelerating Scientific Discovery. *Comput. Sci. Eng.* **2014**, *16*, 62–74.

□ Recommended by ACS

Back to the Basics: Developing Advanced Metal–Organic Frameworks Using Fundamental Chemistry Concepts

Kent O. Kirlikovali, Omar K. Farha, *et al.*

DECEMBER 27, 2022

ACS NANOSCIENCE AU

READ

Giant Redox Entropy in the Intercalation vs Surface Chemistry of Nanocrystal Frameworks with Confined Pores

Jiawei Huang, Carl K. Brozek, *et al.*

MARCH 09, 2023

JOURNAL OF THE AMERICAN CHEMICAL SOCIETY

READ

Exploring the Isoreticular Continuum between Phosphonate- and Phosphinate-Based Metal–Organic Frameworks

Soňa Ondrušová, Jan Demel, *et al.*

NOVEMBER 11, 2022

INORGANIC CHEMISTRY

READ

Mechanochemical Access to Catechol-Derived Metal–Organic Frameworks

Filipp Edvard Salvador, Wen-Yang Gao, *et al.*

FEBRUARY 15, 2023

INORGANIC CHEMISTRY

READ

[Get More Suggestions >](#)